

AD-A174 999

HIGH DENSITY ION IMPLANTED CONTIGUOUS DISK BUBBLE
TECHNOLOGY(U) CARNEGIE-MELLON UNIV PITTSBURGH PA DEPT
OF ELECTRICAL AND COM M H KRYDER SEP 85

1/1

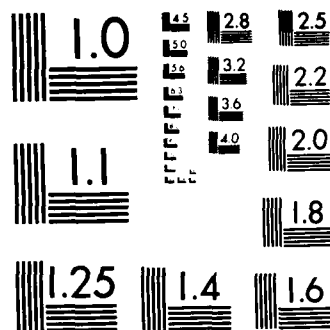
UNCLASSIFIED

AFOSR-TR-86-2210 AFOSR-84-0341

F/G 14/3

NL





MICROCOPY RESOLUTION TEST CHART
NATIONAL BUREAU OF STANDARDS 1963 A

AD-A174 999

AFOSR-84-034/

Title "High Density Ion Implanted
Contiguous Disk Bubble
Technology"~~Ion-Implanted Contiguous Device Design¹~~DTIC
ELECTE
DEC 10 1986

S D

J. R. Wullert II and M. H. Kryder
Department of Electrical and Computer Engineering

Approved for public release (AFOSR)
 Distribution Unlimited
 This report has been reviewed and is
 approved for public release (AFOSR 190-12).
 Distribution Unlimited.
 W. J. ZETTER
 Director, Technical Information Division

Abstract

Ion-implanted contiguous disk bubble memory devices, which were designed and fabricated at Bell Laboratories are being tested. The aim of this testing is to identify the strongest and the weakest elements of these circuits with the hope of designing a fully operational four micron period device. The initial phase of testing has involved obtaining minor-loop propagation bias margins, observing the failure mechanisms and attempting to discover the reasons for these failures. Future work will include similar observation for generation, transfer and detection including both bias and current amplitude and phase margins.

Introduction

The four-micron period ion-implanted devices that were donated to Carnegie-Mellon University possess a variety of different memory and function structures. Some of these device structures have been fully tested for correct operation while others have not. The intent here is to determine both the operating parameter limits and the reasons for them in both the tested and untested circuits. This analysis will provide information that will be used in the design of improved ion-implanted devices. This design process for minor loop propagation is outlined here.

DTIC FILE COPY

¹This work was supported by the Air Force Office of Scientific Research and the National Science Foundation

DISTRIBUTION STATEMENT A
 Approved for public release
 Distribution Unlimited

86 12 09 040

8a. NAME OF FUNDING/SPONSORING ORGANIZATION AFOSR		8b. OFFICE SYMBOL (If applicable) NE		9. PROCUREMENT INSTRUMENT IDENTIFICATION NUMBER AFOSR-84-0341	
8c. ADDRESS (City, State and ZIP Code) Same as 7b				10. SOURCE OF FUNDING NOS.	
		PROGRAM ELEMENT NO. 2305-CT 61102F	PROJECT NO. 2305	TASK NO. C1	WORK UN NO.
11. TITLE (Include Security Classification) Design and Fabrication of Submicron Magnetic Disk					
12. PERSONAL AUTHOR(S) M. H. Kryder Bubble Device Technology					
13a. TYPE OF REPORT Annual		13b. TIME COVERED FROM 9/30/84 TO 9/29/85		14. DATE OF REPORT (Yr., Mo., Day) Sept 85	
15. PAGE COUNT 25					
16. SUPPLEMENTARY NOTATION SEPT-85 Grant Amendment - Research Title Change					
17. COSATI CODES			18. SUBJECT TERMS (Continue on reverse if necessary and identify by block number)		
FIELD	GROUP	SUB. GR.			
19. ABSTRACT (Continue on reverse if necessary and identify by block number)					
<p>Ion-implanted contiguous disk bubble memory devices, which were designed and fabricated at Bell Laboratories are being tested. The aim of this testing is to identify the strongest and the weakest elements of these circuits with the hope of designing a fully operational four micron period device. The initial phase of testing has involved obtaining minor-loop propagation bias margins, observing the failure mechanisms and attempting to discover the reasons for these failures. Future work will include similar observation for generation, transfer and detection including both bias and current amplitude and phase margins.</p>					
20. DISTRIBUTION/AVAILABILITY OF ABSTRACT UNCLASSIFIED/UNLIMITED <input checked="" type="checkbox"/> SAME AS RPT. <input type="checkbox"/> DTIC USERS <input type="checkbox"/>				21. ABSTRACT SECURITY CLASSIFICATION UUU	
22a. NAME OF RESPONSIBLE INDIVIDUAL Dr Gerald Witt		22b. TELEPHONE NUMBER (Include Area Code) 202-767-4931		22c. OFFICE SYMBOL NE	

MTC ANNUAL REPORT

High Density Ion Implanted Contiguous Disk Bubble
~~Ion Implanted Contiguous Device Design~~ *Technology"*

M.H. Kryder

Department of Electrical and Computer Engineering

Carnegie-Mellon University

AFOSR-84-0341

Sept. 84 to Sept 85.



Accession For	
NTIS CRA&I	<input checked="" type="checkbox"/>
DTIC TAB	<input type="checkbox"/>
Unannounced	<input type="checkbox"/>
Justification	
By	
Distribution /	
Availability Codes	
Dist	Avail and/or Special
A-1	

Propagation was chosen as a starting point for two reasons. The first was that it is the simplest of all the bubble memory functions. The second reason was that, at the start of the project, equipment to test the other device functions was not available.

Bias margins were taken for a variety of minor loop structures including the contiguous disk, the snake or zig-zag pattern and two triangular patterns. These patterns are shown in Figure 1 and abbreviated margins for the structures are shown in Table I.

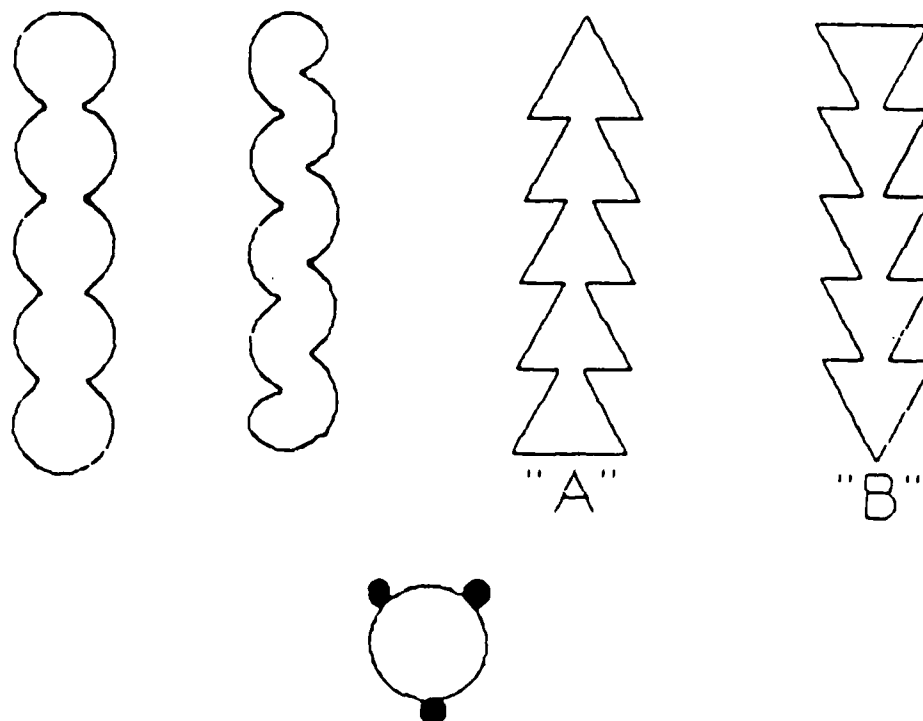


Figure 1: Minor Loop Propagation Patterns

H_{ROT}	Contiguous Disk	Snake	Triangle A	Triangle B
40	450-477	421-456	434-479	424-485
50	426-473	416-449	427-478	432-480
60	416-466	406-435	425-479	431-465(?)

Table 1: Propagation Bias Margins

From the results shown in Table I, one would assume that the triangular patterns, possessing

wider bias margins, are superior to the other patterns. These results are, unfortunately, not directly comparable as will be shown below.

The results shown for the contiguous disk and snake patterns were obtained from minor loops in an actual memory device. The period of the patterns and the spacing between them were both about four microns. Due to the proximity of the loops, a low bias failure in which bubbles would jump from one track to another at the ends of the loops resulted. the exact manner of this failure is shown in Figure 2. This failure was observed only at the ends of the loops positioned away from the major loop. This seemed to indicate that the problem was related to the three-fold symmetry of the material or to stress relaxation. Since the effects of the three-fold anisotropy, when observed on isolated circular patterns, did not seem pronounced in this film, this did not seem likely to be the cause. The large uninterrupted implanted region at the track could lead to stress relaxation, weakening the charged wall there. The charged wall from the cusp is strong and long due to the low bias field and hence grabs the bubble. This results in the low bias failure. At high bias, both of these patterns propagated properly until the bubbles collapsed.

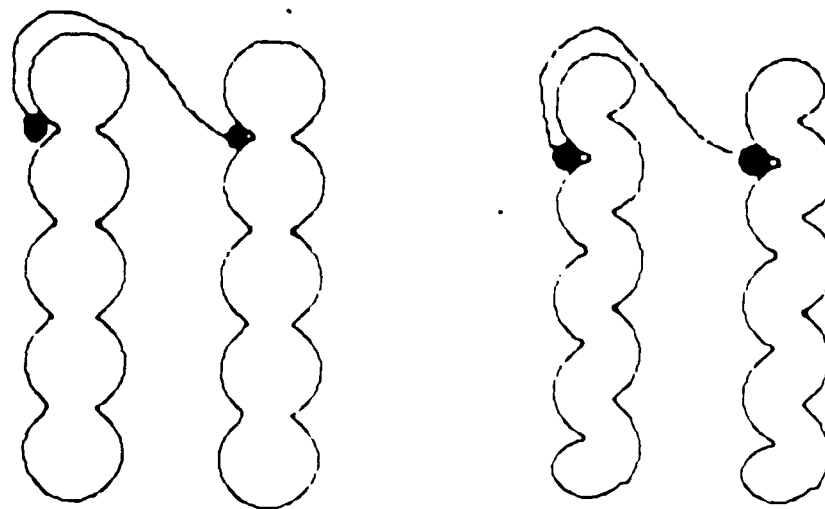


Figure 2: Low Bias Failure Mode

One other point of interest is that the snake pattern seemed to possess significantly more local defects (ie places where bubbles stick). This can not be explained on the basis of lithographic problems as the resolution required for the disk structure is equal to that required for the snake pattern. This could, however, be due to the fact that the cusps on a given snake track are separated by a greater distance than those on the contiguous disk track. This causes the repulsive effect of the opposing cusps on a bubble to be weaker in the snake pattern, providing less force to drive bubbles out of the cusps. Minor variations in stress could then result in bubbles sticking in certain places.

The triangular patterns that were investigated are not located in actual minor loops but in test patterns located about the chip. Although the period of the patterns is again about four microns, the spacing between them is greater; about seven to eight microns. This prevented the low bias failure seen in the snake and disk patterns from occurring. The low bias failure that did show up is, as shown in Figure 3, the stretching of bubbles from cusp to cusp. This failure was more likely to occur on the side of the pattern in which the bubble was propagating up the slope of the triangle, as shown. This indicates that a triangular zig-zag pattern, where the bubble is always propagating up the steep edge, may give better low bias margins.

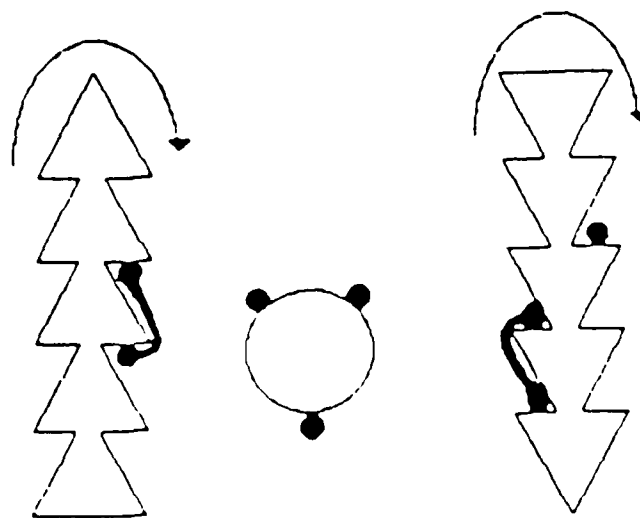


Figure 3: Low Bias Failure Mode

The failure of these structures at high bias was once again bubble collapse, but it occurred invariably as the bubble went around the pointed end of the loop. This is likely to be caused by the fact that the bubble is in contact with very little of the unimplanted region at this point, leading to a weakened effect of the charge wall. This failure could probably be avoided if the corners were more rounded. It should be noted that the high bias margins for pattern B are better (barring the last entry in Table I), which can be related to the fact that pattern B has a preferred bubble position at its point. The last entry in Table I (as marked by a ?) is not really a valid data point as the failure here occurred when the bubbles jumped from the track to an other nearby structure and collapsed there. This type of structure would not be present in an actual circuit.

The two observations made with this analysis lead to the design of a new propagation pattern that possesses the properties discussed. This pattern is shown in Figure 4. This pattern would allow propagation only in the direction indicated but would not be susceptible to the stretch failure that was observed in the triangular pattern. It also possesses rounded corners at the ends of the loops that would increase the high bias margin.

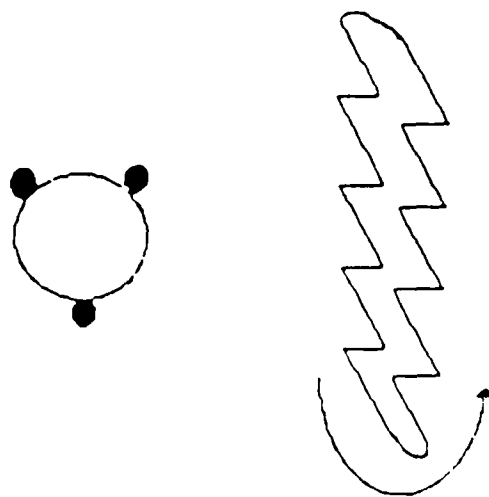


Figure 4: Triangular Zig-Zag Pattern

Work on other bubble memory functions will commence shortly. A microprocessor controlled bubble memory test system donated by Bell Laboratories will allow testing of bias field and current amplitude and phase margins for all functions. This will allow analysis such as that presented here to be done for all areas of ion-implanted devices. The results of these analyses can

be used in a manner that will allow design improvements, again like those presented here, to be made. The end result will be an improved ion-implanted bubble memory device.

Liquid Phase Epitaxial Growth of Garnets¹

R. O. Campbell and M. H. Kryder
Department of Electrical and Computer Engineering

Abstract

A computer modelling system has eased the design of films and provided new film compositions for sub-micron bubble diameter films and isotropic magnetostrictive films. The computer model agrees well with published data and has correctly predicted the properties of standard films. Isotropic magnetostrictive film compositions have been calculated by the computer model and several possible film compositions were shown to have suitable bubble properties. Two different melts have been made, and successful bubble materials with bubble diameters of $0.35\text{ }\mu\text{m}$ have been grown. These films have both of the magnetostriction coefficients negative with λ_{100} more negative than λ_{111} , which is unusual for garnet materials. The magnetostriction measurements were made on [111] and [100] oriented films using a vacuum-stressed FMR apparatus developed here.

¹This work was supported by the Air Force Office of Scientific Research and the National Science Foundation

Introduction

Creation of a computer modelling system has greatly eased film design and provided new film compositions for sub-micron bubble diameter films and isotropic magnetostrictive films. Materials suitable for half-micron bubble diameter ion-implanted contiguous disk (CD) devices have been improved. Two film compositions were developed to provide half-micron to one-micron diameter bubble films.

Isotropic magnetostrictive film compositions have been calculated by the computer model and several possible film compositions were shown to have suitable properties. The incorporation of dysprosium or bismuth seems to be a requirement for isotropic magnetostriction. Several bismuth based and dysprosium doped films have been grown; but have not been used for bubble work at this time.

Several other film compositions have been developed for use in microwave applications and bubble logic devices. The films for microwave use are of a low Q and low $4\pi M_s$ character, unsuitable for bubble applications, while all of the bubble logic films are standard $2\mu\text{m}$ diameter bubble films, as have been grown in past years.

Computer Aided Film/Melt Design Program

The computer aided film design system (CAFE) has been developed to quickly produce film compositions that will satisfy many criteria concurrently. By using the properties of the film constituents such as rare-earths, iron, and iron dilutants, CAFE can extrapolate the hypothetical film properties. Lattice mismatch, magnetostriction coefficients, magnetization, damping, and growth induced and stress induced anisotropies are calculated for any film composition from standard published data.

The magnetostriction coefficients (λ_{111} and λ_{100}), the magnetization, and the damping are calculated using the proportion of each of the rare earths and adjusting for the exchange (A) due to the tetrahedral-octahedral ion pairs. Each rare-earth has associated with it magnetization, damping, and magnetostriction coefficients, so that the net value is the sum of the proportion of each constant. This net value is then decreased due to the exchange which is calculated from the iron dilution.

The lattice mismatch is similarly calculated, however the dilution of the iron sites must be

carefully considered. Typical iron substituents such as gallium and germanium have been installed in CAFE by using a quadratic equation describing the lattice reaction to the dilutant incorporation. The quadratic describes the probability of the ions residing at a tetrahedral site [a smaller site resulting in expansive stress] or an octahedral site [a larger site resulting in compressive stress]. The equations are derived from fitting published data to a curve and approximating the curve numerically.

The growth induced anisotropy is calculated using the pair ordering model of large ion-small ion interaction. A constant K_{ij} is assigned to each pair of rare-earths so that the net growth induced anisotropy is the sum of each K_{ij} -rare-earth product (ie. $K_G = K_{ij} x_Y x_{Lu}$). Anisotropy results from the pair ordering of samarium and europium with other rare-earths have correctly estimated published results. Using the lattice mismatch previously calculated, the stress induced anisotropy is calculated and added to the growth induced anisotropy to find the total uniaxial anisotropy (K_u).

Recently a bismuth anisotropy model has been implemented with mixed results. Bismuth appears to not behave as the pair-ordering model would suggest, but it does have a great effect on anisotropy. The bismuth anisotropy implementation should be completed within the year.

Choosing a Q and a bubble diameter, the values of A , K_u , and $4\pi M_s$ can be determined from two standard bubble equations. First, the ratio of K_u to $2\pi M_s^2$ is equal to Q

$$Q = K_u / 2\pi M_s^2$$

and secondly, the characteristic length (l) is directly related to the bubble diameter, the exchange constant (A), the anisotropy constant (K_u), and the magnetization ($4\pi M_s$) by:

$$l = 16\pi (A K_u)^{1/2} / (4\pi M_s)^2 = (\text{bubble diameter})/9$$

CAFE will find suitable film compositions given any Q , bubble diameter, and choice of film constituents by scanning all possible film compositions and retaining only those that satisfy all requirements.

Film Growth Technique

All garnet film growth is by the standard vertical dipping method. Non-bismuth films are grown from a platinum crucible that contain a solution of the film's constituents dissolved in a $\text{PbO-B}_2\text{O}_3$ flux (the melt). This solution is super heated to above the saturation temperature (T_{sat}) and allowed to homogenize for a minimum of 24 hours.

The films are grown by decreasing the temperature below T_{sat} (typically 880°C) and lowering a $\text{Gd}_3\text{Ga}_5\text{O}_{12}$ (GGG) substrate rotating at 100 RPM into the melt. The substrate is allowed to reach the melt temperature before being inserted into the melt. The film will grow as long as the melt temperature is below T_{sat} and the mismatch between the film and the substrate is not too great: typically less than 0.03A. The film is grown approximately $0.1\mu\text{m}$ thicker than the bubble diameter; thus for a $1\mu\text{m}$ diameter bubble film, the thickness would be $1.1\mu\text{m}$. Typical growth rates (dependent upon super-cooling) are $0.2\mu\text{m}/\text{min}$ to $0.5\mu\text{m}/\text{min}$, so that growth times vary from 2 minutes to 10 minutes. After the film is grown, the substrate must be dismounted from the platinum holder and any remaining PbO flux drops must be dissolved.

A 40% acetic acid, 10% nitric acid, 50% water solution proved effective for removing $\text{PbO-B}_2\text{O}_3$ flux from the substrate and substrate holder. This flux removing solution was found to be insufficient when removing the $\text{PbO-Bi}_2\text{O}_3$ flux used for growing bismuth doped films. The flux removing solution was systematically altered to 40% acetic acid, 40% nitric acid, 20% water which proved to remove all of the remaining flux. During the flux removal procedure, the substrate, while mounted on the substrate holder is alternately placed on heat (90°C) and submerged in an ultrasonic bath.

Characterization Techniques

The grown films are characterized for possible melt alteration as well as to provide data for device work. Every film grown has its thickness measured, while most have the characteristic length and magnetization measured. Sample films are further characterized for lattice mismatch, damping, gyromagnetic ratio, magnetostriction coefficients, and H_k .

The thickness measurements are made optically from a reflectance trace of the film. Using the interference of the light reflected from the bottom surface and the top surface of the film, a reflectance trace of the film is made by varying the wavelength of the incident light. This trace can then be used with a curve of the index of refraction as a function of the light's wavelength to

determine the thickness. This results in a fast nondestructive measurement of the thickness that relies on one destructive measurement which determines the index of refraction curve using a surface profilometer.

Both the characteristic length (l) and the magnetization ($4\pi M_s$) are found optically by domain observation. l is found by measuring the strip width of a demagnetized sample. $4\pi M_s$ is found by determining the perpendicular field that causes the bubbles to collapse and by calculating the ratio of stripe width to film thickness. Published tables relate the ratios of strip width and film thickness to the collapse field and $4\pi M_s$.

Using ferromagnetic resonance (FMR) we can calculate the gyromagnetic ratio, gilbert damping parameter, effective field, and magnetostriction coefficients. By finding the resonance of the sample at various microwave frequencies, a curve of resonant frequency versus applied field is constructed. The slope of the curve is the gyromagnetic ratio, and the Gilbert damping parameter is related to the linewidth of the resonance. The effective field is similarly found. Furthermore, by stressing the sample mechanically, the magnetostriction coefficients can be determined. The stress is produced mechanically by a vacuum applied to one side of the substrate. The shift in the resonant field can be related to the magnetostriction constants. This method will be used to verify that films are isotropic magnetostrictively.

The lattice mismatch is measured using a double crystal X-ray diffractometer. The X-rays penetrate approximately $4\mu\text{m}$ into the garnet, thus going through the film to the substrate. Peaks are observed at the two angles corresponding to the substrate's lattice spacing and the film's lattice spacing. The difference of the angles is measured and used to determine the lattice mismatch, and from the relative intensities of the peaks, the thickness is approximated.

Current Materials Development

Two submicron film compositions have been developed. The first melt produced films of $(\text{Sm}_{0.65}\text{Gd}_{2.40}\text{Tm}_{1.0}\text{Y}_{0.8}\text{Lu}_{0.27}\text{Fe}_{4.8}\text{Ga}_{0.2})$ with an l value of $0.056\mu\text{m}$ for a bubble diameter of $0.504\mu\text{m}$.

A second melt producing films of $(\text{Sm}_{1.2}\text{Lu}_{1.7}\text{Tm}_{0.1}(\text{FeGa})_5\text{O}_{12})$ was also developed for sub-micron bubbles. Data from films typical of the melt, AC21, AC22, AC32 are shown in Table 1. This melt required significant alterations including an addition of gallium and iron to adjust the

strip width (l) from $0.08\mu\text{m}$ to $0.06\mu\text{m}$. The films were grown with a super cooling of 20°C and a T_{sat} of 880°C . These films have been shown to successfully demonstrate propagation of $0.5\mu\text{m}$ bubbles in $2\mu\text{m}$ period contiguous disk devices.

Present work is centered on developing a bubble material with isotropic magnetostriction suitable for ion-implanted contiguous disk (CD) devices. For CD devices the magnetostriction coefficients must be negative, and as large as possible. Most rare-earth ions have λ_{111} less than λ_{100} , so that a balancing ion with λ_{111} greater than λ_{100} must be used. Two such balancing ions are being investigated for use; dysprosium, with $\lambda_{111} = -5.90$ and $\lambda_{100} = -12.60$, and bismuth with $\lambda_{111} = +15.5$ and $\lambda_{100} = +8.20$. Thus dysprosium may be used without making the coefficients positive; however, dysprosium has a damping that is about forty times greater than the standard rare-earths. By using both dysprosium and bismuth together in a film, we will be able to satisfy the isotropic magnetostriction requirements and have large negative magnetostrictive coefficients and maintain a reasonable damping. Two sets of films have been grown from two different flux based melts: the first melt was a dysprosium doped standard $\text{PbO-B}_2\text{O}_3$ flux melt and the second melt was a bismuth $\text{PbO-Bi}_2\text{O}_3$ flux melt.

The Dysprosium film composition was to be $(\text{Sm}_{0.3}\text{Dy}_{1.6}\text{Gd}_{0.4}\text{Lu}_{0.7}(\text{FeGa})_5\text{O}_{12})$ which would have magnetostriction coefficients of -2.8×10^{-6} and a mismatch of less than 0.005 Å. Films were grown from this melt; however, the films were not useful for device work.

The second isotropic magnetostrictive melt was based on the bismuth system. The incorporation of bismuth into the film has several advantages including an increase of optical contrast due to an increase of the Faraday rotation, a secondary source of anisotropy, and a correction of magnetostriction. Due to bismuth's positive magnetostriction coefficients, ($\lambda_{111} = +15.50$ and $\lambda_{100} = +8.20$), bismuth is used in small quantities as a correction to the magnetostriction. The greatest difficulty with using bismuth is that a new flux system must be developed employing $\text{PbO-Bi}_2\text{O}_3$ instead of $\text{PbO-B}_2\text{O}_3$. We have previously had little experience and no success with this system.

We have grown films of a bismuth doped nature ($\{\text{Dy Sm Lu Y Bi}\}_{3.0}[\text{Fe}]_5\text{O}_{12}$), and several films have been fully characterized. However, the properties are not yet suitable for bubble devices: the magnetization is larger than desired ($4\pi M_s = 1750\text{G}$) and the bubble diameter is smaller than desired at $0.35\mu\text{m}$. The magnetostriction coefficients are promising with $\lambda_{100} =$

-4.6×10^{-6} and $\lambda_{111} = -1.8 \times 10^{-6}$; the fact that λ_{100} is more negative than λ_{111} shows that the melt is over compensated for isotropic magnetostriction.

A difficulty with the bismuth films is the non-uniformity of the surface. This is due to the flux adhering to the film while being being withdrawn from the melt letting the film continue to grow until the flux drops solidify. These flux drops result in a thicker film where the flux drops remain after withdrawal. Solving this problem was accomplished by adding Vanadium to the melt so that the surface tension of the melt was increased while the melt viscosity was decreased.

Standard bubble materials for bubble logic devices and micro-wave use have also been grown. The bubble logic materials are standard $2\mu\text{m}$ bubble diameter films. Several $2\mu\text{m}$ bubble systems have been developed in the past by Charles Krafft. The microwave material was developed for research of microwave generated ring domains. The required material was of composition $(\text{Y}_{3-x}\text{La}_x\text{Fe}_{5-y}\text{Ga}_y\text{O}_{12})$ where x is approximately 0.2 and y approximately 1.2. These films had an extremely small magnetization of less than 250 Oe. This resulted in a small Faraday rotation and poor optical contrast due to the relation between $4\pi\text{Ms}$ and Faraday rotation. Typical film properties are listed in Table 1.

Conclusion

The development of CAFE for modeling film compositions is very successful and has enabled a greater variety of compositions to be studied. Agreement with published results is good for the standard garnet constituents. Development of sub-micron materials is proceeding well and films have been used for ion-implanted contiguous disk devices. Film designs with isotropic magnetostriction have been created by CAFE and bismuth based and dysprosium doped films have been grown with an isotropic nature. A working isotropic magnetostrictive melt for CD devices should be developed in the near future.

STRESSES AND MAGNETOELASTIC ANISOTROPIES AT IMPLANTATION EDGES IN ION-IMPLANTED GARNET FILMS

D. A. Saunders and M. H. Kryder

Department of Electrical and Computer Engineering
Carnegie-Mellon University, Pittsburgh, Pa. 15213

Abstract

Stresses at the edge of an ion-implanted region in a magnetic garnet film have been calculated by analogy with thermal-induced stresses in an elastic half-space. From these stresses, magnetoelastic anisotropies have been computed for two different implant profiles and for straight and beveled mask edges. The model shows that stress relaxation in the vicinity of an implantation edge decreases with distance from the edge with an exponential decay length of approximately $4t$, where t is the implantation layer thickness. Stress perpendicular to the film surface and shearing stress are significant at the implantation edge, but decrease more quickly with decay lengths of approximately $.8t$ and $.6t$, respectively. Because of perpendicular and shearing stresses, the anisotropy under the edge of the implantation mask is found to favor planar magnetization. For similar reasons, the anisotropy in the implanted region near the mask edge is found to favor perpendicular magnetization, effectively causing a shift in the mask edge toward the $[11\bar{2}]$ direction. The shift is especially evident in materials with $\lambda_{111} \neq \lambda_{100}$ and is on the order of $2.5t$ for a material with $\lambda_{111} = -\lambda_{100}$. The anisotropy distribution near a beveled mask edge indicates that a charged wall may not be well-defined along such an edge.

PACS numbers: 85.70.Ec, 85.70.Ge

Introduction

As first outlined by Hidaka and Matsutera¹, relaxation of ion-implantation-induced stress at the interface between implanted and unimplanted regions in contiguous-disk bubble devices leads to the formation of charged walls used for bubble propagation. The stress relief gives rise to a large, uniaxial, magnetoelastic anisotropy parallel to the implantation edge which stabilizes the charged walls. Other stresses present can also greatly affect the magnetization behavior². In this paper the stresses in the vicinity of boundaries between implanted and unimplanted regions of a garnet are calculated and used to find the variation of magnetoelastic anisotropies with position. Stable magnetization directions as a function of position are calculated by energy minimization of the various anisotropy energies at those positions.

Elastic Model

In the elastic model, the implanted ions are treated as "centers of dilatation" which push outwardly in all directions from their positions in a uniform, elastic half-space, i.e. the garnet film and substrate. From this point of view, the expansion due to implantation is analogous to the thermal expansion due to a temperature rise. By this analogy the calculations of Ignaczak and Nowacki³ are used to model the stresses around rectangular implanted patterns in a garnet film. The garnet is assumed to be elastically isotropic and completely described by Poisson's ratio, ν . The strength and density of the implanted ions and the Young's modulus of the garnet are all taken into account by choosing the planar stress, σ_p , present in the regions far from the implant masks. All stresses present in the garnet are then normalized to this planar stress.

An implant with uniform ion density throughout its depth, t , is used as the reference implant. It is defined as causing a planar stress, σ_p , which leads to a planar anisotropy, Q_{US} . For comparison, a 200 keV neon ion implant is modeled as a ten-layer, piecewise-uniform implant which varies with depth as determined by MacNeal and Speriosu⁴. The neon implant is scaled to have the same total dosage as the uniform implant. To investigate the effect of a poorly defined mask edge, a beveled-edge implant is also simulated here as a uniform implant having a 45° stepped edge made up of ten steps.

The coordinate system for the stresses near to a long, straight mask edge is shown in Fig. 1. For the purpose of calculating the magnetoelastic anisotropies (Eq. 1), it is only necessary to deal with the normalized, differential stresses, $S_2 = (\sigma_y - \sigma_x)/\sigma_p$ and $S_3 = (\sigma_z - \sigma_x)/\sigma_p$, and the normalized shear stress, $S_{13} = \sigma_{xz}/\sigma_p$.

Magnetic Model

The orientation of the magnetization at the edge of an implanted region was found by minimization of the various anisotropy and magnetostatic energies as given in the following equation:

$$\begin{aligned}
 E = & -(Q_U - 1) \cos^2 \theta \\
 & + Q_{US} \{ [-S_3 + S_2 (\Delta/6)] \cos^2 \theta \\
 & - [S_2 (1 - \Delta/3)] \sin^2 \theta \sin^2 \phi \\
 & - [S_2 (\sqrt{2}\Delta/6)] \sin 2\theta \sin(\phi + 3\psi) \\
 & - [S_{13} (1 - 2\Delta/3)] \sin 2\theta \cos \phi \\
 & + [S_{13} (\sqrt{2}\Delta/3)] \sin^2 \theta \sin(2\phi + 3\psi) \} \\
 & + Q_1 \{ (\sin^4 \theta)/4 + (\cos^3 \theta)/3 + (\sqrt{2}/3) \sin^3 \theta \cos \theta \cos 3(\phi + \psi) \} \\
 & - \{ H_X \sin \theta \cos \phi + H_Y \sin \theta \sin \phi + H_Z \cos \theta \} / 2\pi M
 \end{aligned} \tag{1}$$

where Q_U is the perpendicular uniaxial anisotropy, $K_U/2\pi M^2$; Q_{US} is the magnetoelastic planar anisotropy due to implantation, $1.5\lambda_{111}\sigma_p/2\pi M^2$ (the change in perpendicular Q was assumed to be totally due to implantation stress); Δ is the anisotropic magnetostriction constant, $(\lambda_{111} - \lambda_{100})/\lambda_{111}$; Q_1 is the magnetocrystalline anisotropy, $K_1/2\pi M^2$, H_X , H_Y , and H_Z are the fields along the axes of Fig. 1, M is the magnetization; θ and ϕ are the angles of the magnetization as shown in Fig. 1; and ψ is the angle of the

mask edge as in Fig. 1.

Using the stress distributions calculated from the elastic model, the distributions of the magnetization near to the implant mask edge were calculated for varying material parameters. Exchange interactions and demagnetizing effects were not included in the model (except for a thin-film demagnetizing term) and, therefore, the distributions are due only to the spatial variation of the stress. The spacing of the magnetic dipoles on the grid is such that exchange effects could cause noticeable interaction between adjacent dipoles along the z-direction but little interaction along the x-direction. Demagnetizing fields would also alter the magnetization distributions shown here, but the magnetoelastic anisotropies are generally large enough to resist demagnetization (as evidenced by the formation of charged walls). In some of the magnetization distributions shown here, dipoles can be found which are not oriented like any of their neighbors. Generally, this is because the energy minimization routine has found a relative minimum rather than the absolute minimum or, in the case of the beveled (stepped) edge, that dipole is near to the corner of one of the implantation steps.

Uniform Implant

Shown in Fig. 2 are plots of S_2 , the "stress relief" perpendicular to the mask edge; S_3 , the differential stress perpendicular to the film plane; and S_{13} , the shear in the xz-plane, for an implant uniform with depth. In Fig. 3 is shown the magnetization distribution due to this implantation in a magnetostrictively isotropic film ($\Delta=0$). (Note that the vertical axis and horizontal axis are not equally scaled in these figures and that the distances are given in implantation depths, t .) It can be seen that the magnetization is quite planar and is aligned parallel to the mask edge throughout most of the implanted region, except at the bottom corner of the implant near to the mask edge. This is due to the decrease in stress relief, S_2 , and the increases in perpendicular stress, S_3 , and shear stress, S_{13} , in this area. Thus, the easy axis parallel to the mask edge and the planar anisotropy are weakened, while a strong easy axis of magnetization is induced at 45° from the film normal by S_{13} . This region does not extend very far from the mask edge, but it does indicate that a charged wall is more likely to reside near the surface of a film close to the mask edge.

Another significant characteristic of Fig. 3 is the formation of a planar "edge domain" just under

the lip of the mask within the unimplanted region. This is mainly due to the negative peak in S_3 in this area. Also, S_2 is negative in this area, inducing a hard axis parallel to the mask edge so that the magnetization lies perpendicular to the mask edge. In general, these domains are not seen (if indeed they exist) in most films; however, we have observed such domains in at least one film.

For an edge at $\psi=90^\circ$ and $\Delta>0$ (Fig. 4), the easy axis parallel to the edge is weakened via the S_2 term and the second S_{13} term in Eq. 1. This causes the planar magnetization region to shift outward from the mask edge: about .5t, 1.3t and 2.5t for $\Delta=1, 1.5$ and 2, respectively. At $\psi=-90^\circ$ and $\Delta>0$ (no figure), the S_{13} -induced anisotropy is of the opposite sign, strengthening the easy axis parallel to the mask edge near the implantation depth where S_{13} dominates. There the planar region is shifted inward under the mask edge (though less so than the outward shift at $\psi=+90^\circ$.)

200 keV Neon Implant

Because the 200 keV implant has a wide peak, the magnetization distributions due to the neon implant (Fig. 5) are not very different from those due to the uniform implant. However, because the less well-defined implantation depth (the tail of the implant) reduces the shearing at the mask edge, the magnetization in the implanted region for $\Delta=0$ is more planar at the edge than in Fig. 3. Distributions for $\Delta>0$ and $\psi=90^\circ$ and -90° are not shown here but have been generated. These indicate that a charged wall is more likely to reside near the bottom of this implant and that the planar region is less shifted from the mask edge for the profiled implant. However, sharper implant profiles may have larger shearing stresses and increased shifting of the planar region from the mask edge.

Beveled Edge Implant

The magnetization distribution at a beveled edge for $\Delta=0$ (not shown) has, as one might expect, a beveled planar region. The bevel of the planar region essentially follows the bevel of the implant. The distribution for $\Delta=1$, $\psi=90^\circ$ is shown in Fig. 6. Here the planar edge is slightly more beveled than the $\Delta=0$ case and a charged wall may be poorly defined. For $\Delta=1$, $\psi=-90^\circ$, the planar region is less beveled than the $\Delta=0$ case.

Conclusions and Suggestions

It is shown here that an implant uniform in depth does not lead to magnetization uniform in depth near to the mask edge. If uniform magnetization is desired and if $\Delta=0$, the implant should be uniform throughout most of the depth and then taper off into the bulk (most "uniform" implants are like this anyway). If $\Delta \neq 0$, the implant should peak slightly near the surface to increase the reduced "stress-relief anisotropy". Implants with smooth peaks deep in the drive layer may have the advantage of causing more uniform stress relief, S_2 , and allowing the charged wall to reside near to the bubble layer. However, peaked implants do not give uniform planarity, and a charged wall in such an implanted film may vary greatly with depth. Because the implantation of heavy ions induces planar magnetization primarily through magnetostriction⁵, heavy ion implants can produce "edge shifting": perpendicular magnetization near the mask edge due to the peak in σ_z . However, light ions such as hydrogen and deuterium produce additional planar anisotropy to suppress the edge shift. For this reasons, the use of lighter ions, such as hydrogen and deuterium, may be preferable. Some mixing of heavy and light ions could also be done to separately tune the distribution of stress and the planarity of magnetization.

Acknowledgements

The authors wish to thank P. Asselin for proposing the elastic model utilizing the centers of dilitation.

1. Y. Hidaka and H. Matsutera, "Charged Wall Formation Mechanisms in Ion-Implanted Contiguous Disk Bubble Devices," *Applied Physics Letters*, **39** No. 1, 116 (1982)
2. M.H. Kryder and D.A. Saunders, "The Effects of Stress Relaxation and Anisotropic Magnetostriction on Charged Walls in Ion-implanted Garnets," *IEEE Trans. Mag.*, **Mag-15**, No. 5, 1817 (1983).
3. J. Ignaczak and W. Nowacki, "Two Cases of Discontinuous Temperature Field in an Elastic Space and Semi-Space," *Bulletin of the Polish Academy of Sciences, Technical Science Series*, **VI**, No. 6, 309 (1958).
4. B. E. MacNeal and V.S. Speriosu, "Modelling Strain Distributions in Ion-Implanted Magnetic Bubble Materials," *Journal of Applied Physics* **52**(6), 3935 (1981)
5. C.S. Krafft, M.H. Kryder and J.O. Artman, "Annealing Behavior of Deuterium Implanted Films", *IEEE Trans. Mag.*, **MAG-20**, No. 5 1111(1984)

Figure Captions

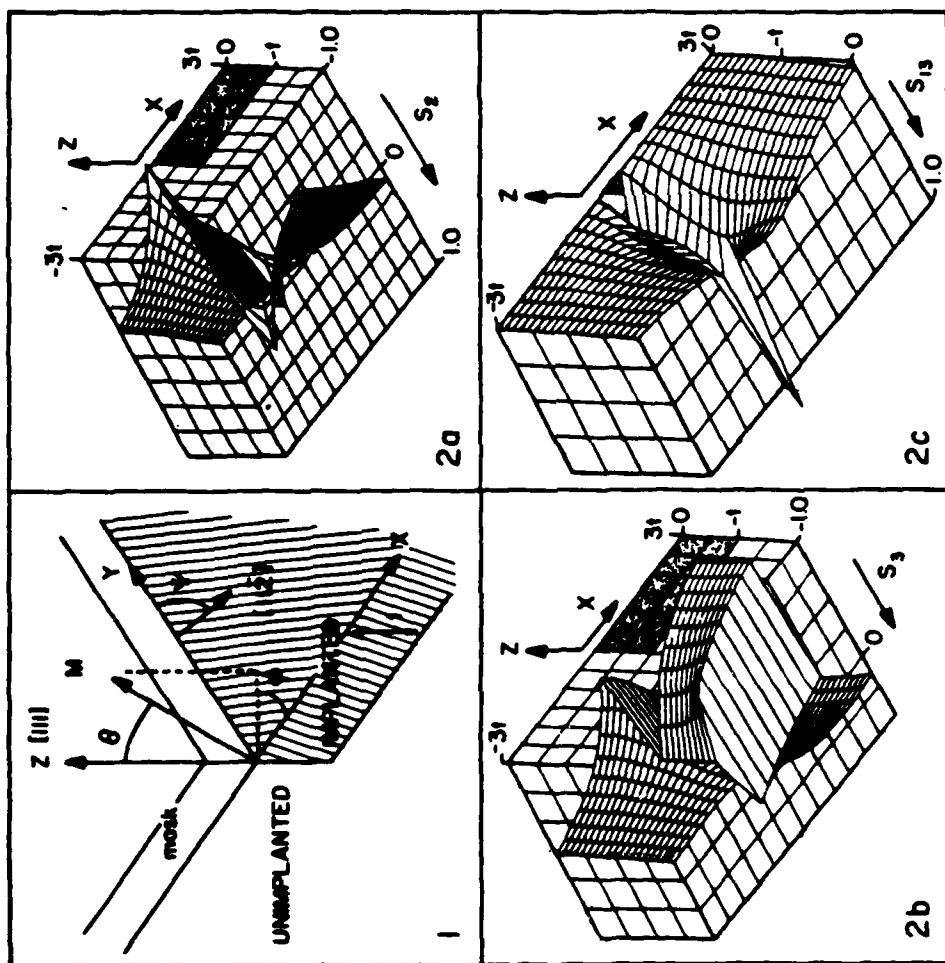
FIG. 1. Coordinate system of Eq. 1. FIG. 2. (a) Stress Relief, S_2 , (b) differential stress, S_3 , and (c) shearing stress, S_{13} as functions of position. Shaded areas indicate implanted regions.

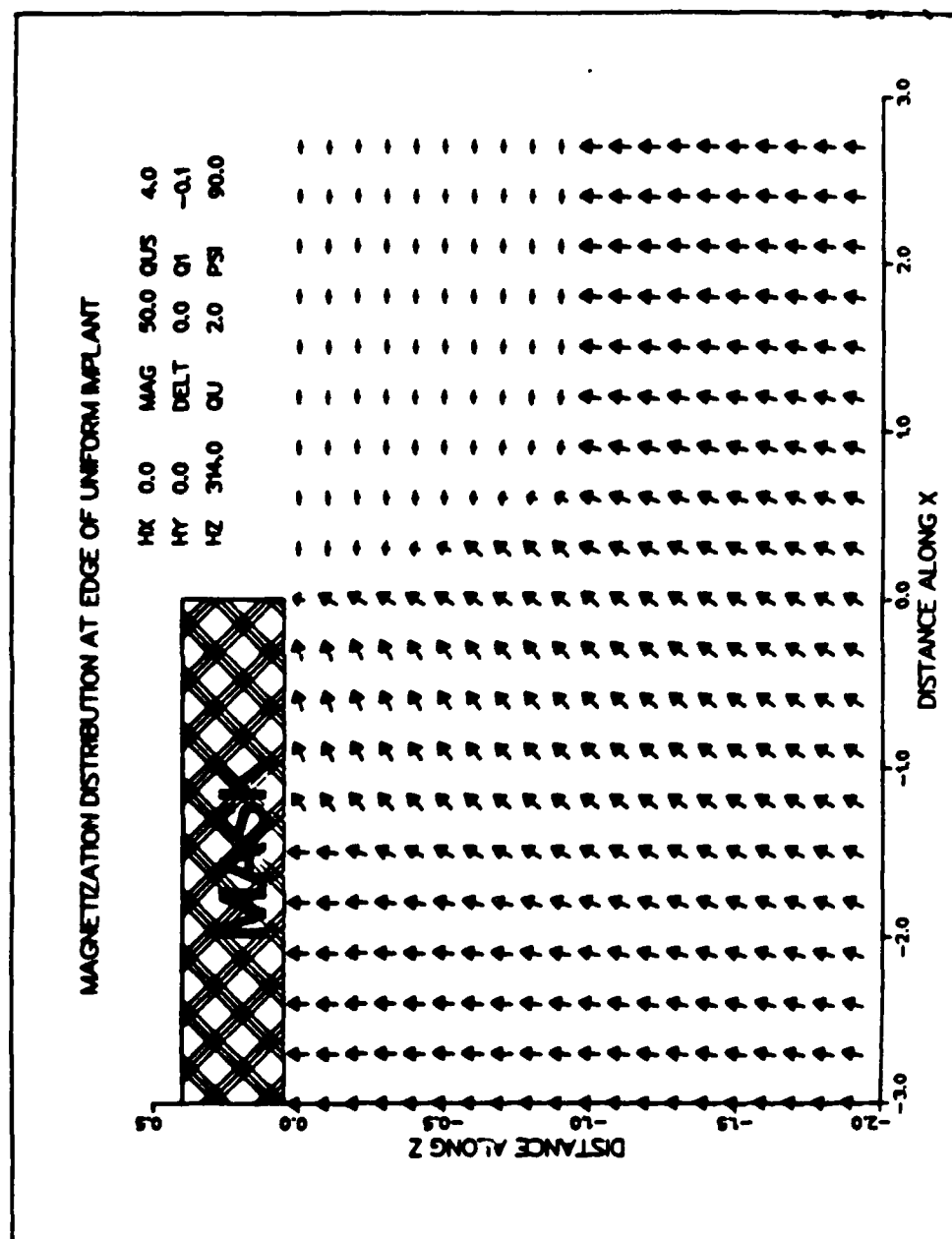
FIG. 3. Orientation of magnetization at mask edge for a uniform implantation, $\Delta(\text{DELT})=0$.

FIG. 4. Orientation of magnetization at mask edge: uniform implant, $\Delta=1$, $\psi=90^\circ$.

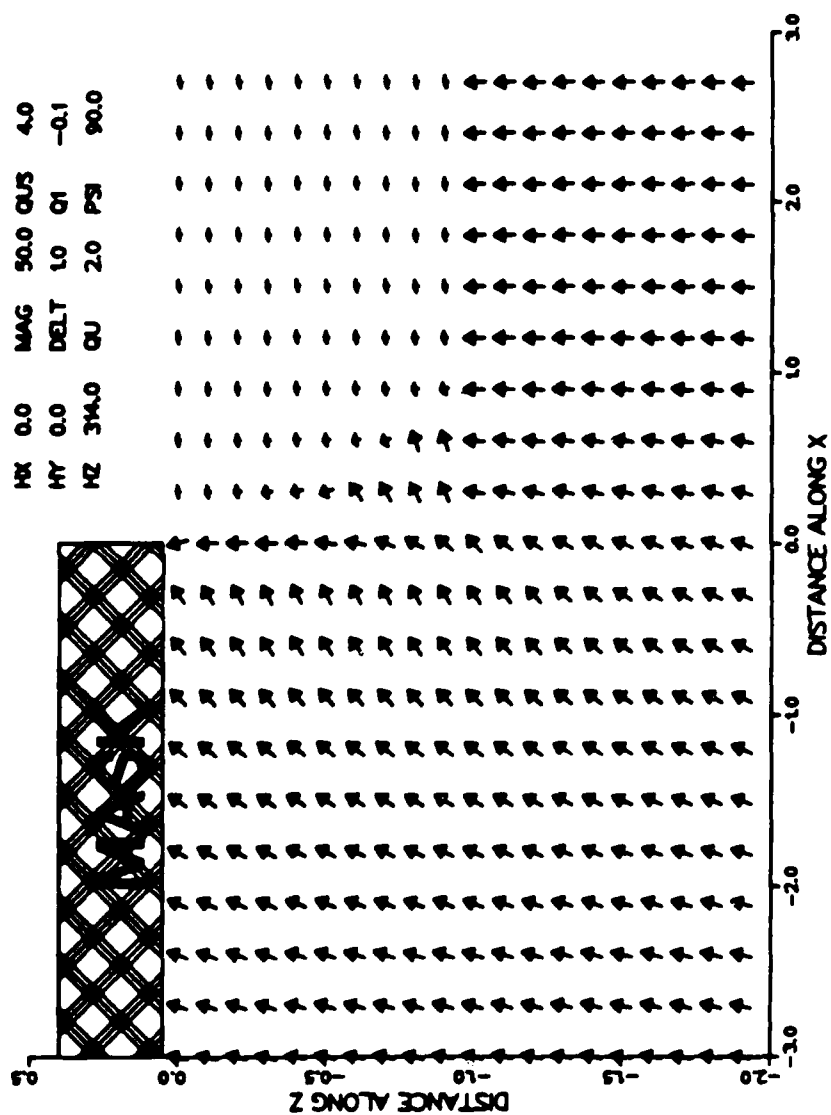
FIG. 5. Orientation of magnetization at mask edge: neon implant, $\Delta=0$.

FIG. 6. Orientation of magnetization at beveled mask edge: $\Delta=1$, $\psi=90^\circ$.





MAGNETIZATION DISTRIBUTION AT EDGE OF UNIFORM IMPLANT



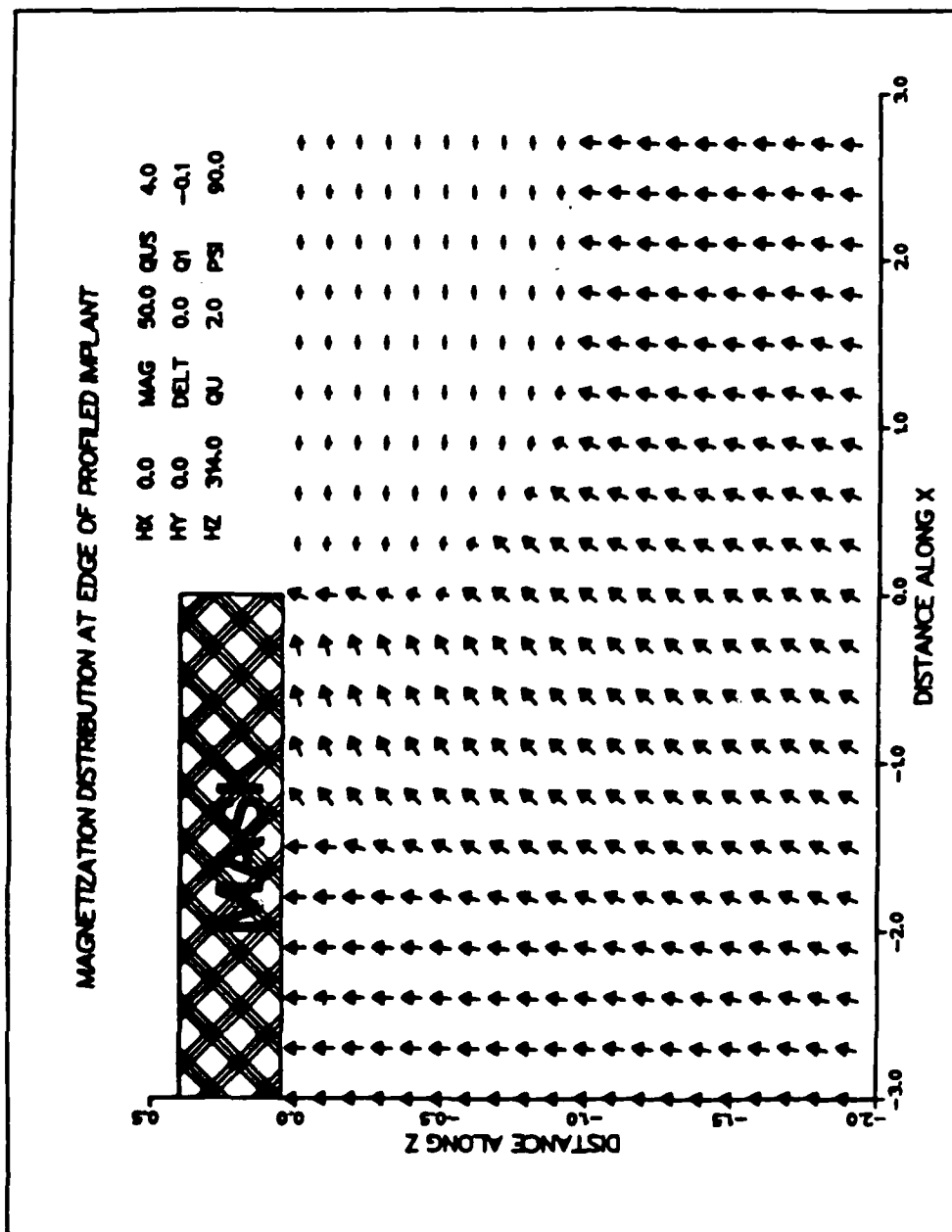
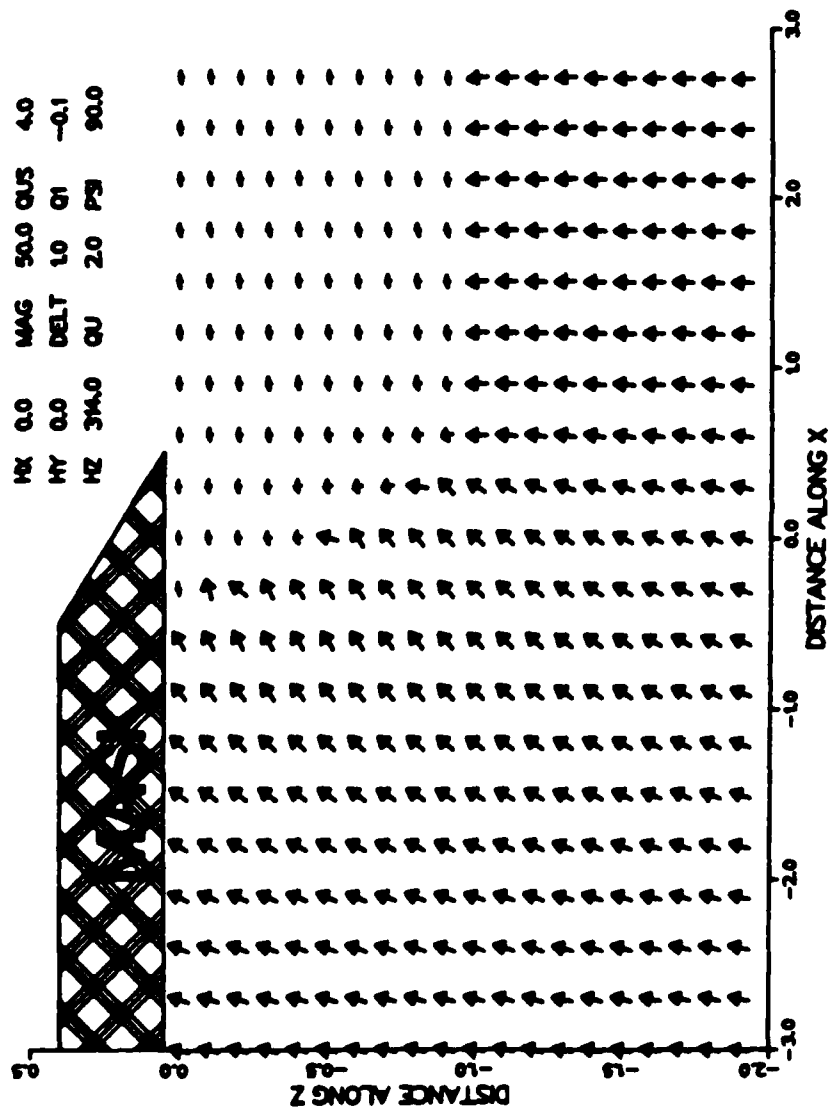


Fig. 5

MAGNETIZATION DISTRIBUTION AT EDGE OF BEVELED IMPLANT



END

1-87

DTIC